ORNL/TM-11102

ornl

OAK RIDGE
NATIONAL
LABORATORY

MARTIN MARIETTA

A First Glance at the Initial ATF Experimental Results

B. A. Carreras
N. Dominguez
J. N. Leboeuf
V. E. Lynch
L. A. Charlton

OAK RIDGE NATIONAL LABORATORY
CENTRAL RESEARCH LIBRARY
CIRCULATION SECTION
4500N ROOM 175
LIBRARY LOAN COPY
DO NOT TRANSFER TO ANOTHER PERSON
If you wish someone else to see this report, send in name with report and the library will arrange a loan.

OPERATED BY
MARTIN MARIETTA ENERGY SYSTEMS, INC.
FOR THE UNITED STATES
DEPARTMENT OF ENERGY

ORNL/TM-11102
Dist. Category UC-427

Fusion Energy Division

A FIRST GLANCE AT THE INITIAL ATF EXPERIMENTAL RESULTS

B. A. Carreras
N. Dominguez
J. N. Leboeuf
V. E. Lynch*
L. A. Charlton*

*Computing and Telecommunications Division, Martin Marietta Energy Systems, Inc.

DATE PUBLISHED: May 1989

Prepared by
OAK RIDGE NATIONAL LABORATORY
Oak Ridge, Tennessee 37831
operated by
MARTIN MARIETTA ENERGY SYSTEMS, INC.
for the
U.S. DEPARTMENT OF ENERGY
under contract DE-AC05-84OR21400

MARTIN MARIETTA ENERGY SYSTEMS LIBRARIES

3 4456 0299804 0

CONTENTS

ABSTRACT v

1. INTRODUCTION 1

2. EQUILIBRIUM PROPERTIES OF THE ATF-A CONFIGURATION . . 3

3. IDEAL MHD STABILITY PROPERTIES OF THE ATF-A CONFIGURATION 9

4. FLUCTUATION LEVEL IN ATF-A CAUSED BY RESISTIVE PRESSURE-GRADIENT-DRIVEN TURBULENCE 14

5. LOW-n RESISTIVE INTERCHANGE INSTABILITY IN ATF-A 21

6. DISCUSSION AND CONCLUSIONS 25

ACKNOWLEDGMENT 27

REFERENCES 29

ABSTRACT

In the initial phase of ATF operation, the plasma minor radius and the edge rotational transform were reduced by field errors. This caused an effective change of the magnetic configuration: it improved the stability properties but worsened the equilibrium properties. The threshold for the second stability regime was lowered to $\beta_0 \sim 1.5\%$. Experimental profile data are compatible with operation in the second stability regime, and the achieved beta values, $\beta_0 \sim 3\%$, are well beyond the theoretically calculated threshold. Magnetic fluctuation measurements showed the effects of beta self-stabilization. They are in reasonable agreement with the predictions of the theory and support the evidence that ATF has already operated in the second stability regime.

1. INTRODUCTION

The Advanced Toroidal Facility (ATF)[1] is a stellarator designed to have stable access to the second stability regime.[2,3] That is, the magnetic axis shift of this configuration as a function of beta is large enough to offset the destabilizing effect of the increased pressure gradient.[4] The second stability regime is defined in relation to ideal magnetohydrodynamic (MHD) stability, and it is relevant only to pressure-gradient-driven instabilities. In the second stability regime, resistive modes can be, and in general are, unstable. That is the case of the resistive interchange instability.[5] In ATF, access to the second stability regime is achieved by a combination of magnetic well and shear. The shear in the plasma edge region is large enough to stabilize the ideal interchange modes, but it reduces the linear growth rate of the resistive interchange only slightly. However, this does not imply that resistive pressure-driven instabilities are not affected by operation in the second stability regime. As beta increases, the magnetic well broadens and reduces the radial range of the resistive interchange instability. The saturation level of the resistive interchange is reduced with increasing beta when the plasma is in the second stability regime. Therefore, measurements of the fluctuation levels associated with this instability give an indication of when the second stability regime has been accessed. Furthermore, since the resistive interchange is a likely candidate to explain the anomalous transport at the edge of stellarator plasmas, this reduction of the fluctuation level with beta should cause an improvement in confinement. The impact on confinement of operation in the second stability regime for ATF is discussed in detail in Ref. 6.

In the initial phase of ATF operation the plasma utilization volume was less than expected because of some field errors,[7] which have since been repaired. These field errors effectively reduced the plasma minor radius and the rotational transform ι at the plasma edge. For convenience, we refer to this modified ATF configuration as the ATF-A configuration. The parameters of ATF-A are compared to the expected ATF parameters in Table I. The combination of reduced rotational transform and increased aspect ratio produces a considerable increase in the magnetic axis shift as a function of beta. The increase can be as much as a factor of six over that expected for the ATF standard configuration. As a consequence, the stability properties of the ATF-A configuration are better than those of the standard configuration, but its equilibrium properties are poorer. In practice, this is reflected in a reduction of the beta threshold for the second stability regime to about $\beta_0 \sim 1.5\%$ and a

Table I. Parameters of the ATF and ATF-A Configurations

Configuration	A_p	$\iota(a_p)$	$\iota(a_p)^2/A_p$	β_0 for 50% shift	β_0 for which min $\iota(r) = 0$
ATF	7.2	1.0	0.139	0.08	0.16
ATF-A	11.0	0.5	0.023	0.02	0.05

decrease of the equilibrium beta limit. This change of the MHD properties makes the ATF-A configuration a very interesting one for the study of plasma stability without the requirement of high power levels.

In the first phase of operation, only a limited number of diagnostics were installed on ATF. As a consequence, the available experimental data are sparse, and there is no conclusive experimental evidence of access to the second stability regime. However, magnetic fluctuation measurements[8] suggest that this regime was reached. We investigate the properties of the ATF-A configuration using the available pressure profile data. We also calculate the fluctuation level for the resistive interchange as a function of beta and compare it with the magnetic fluctuation measurements. The goal is to answer the question: are the present ATF data compatible with operation in the second stability regime?

The remainder of this paper is organized as follows. In Sect. 2, the equilibrium properties of the ATF-A configuration are studied; the corresponding ideal MHD stability properties are discussed in Sect. 3. The local density and magnetic fluctuation levels of resistive pressure-gradient-driven turbulence are evaluated in Sect. 4, and their dependence on beta in the second stability regime is discussed in detail. In Sect. 5, the fluctuation level of low-n saturated resistive interchange modes is calculated, and predictions for edge poloidal magnetic field fluctuations are given. Finally, in Sect. 6, the overall stability picture for ATF with field errors is discussed and the conclusions are stated.

2. EQUILIBRIUM PROPERTIES OF THE ATF-A CONFIGURATION

To analyze the MHD equilibrium properties of the ATF-A configuration, we use some of the available experimental information, namely, the vacuum magnetic axis position and the pressure profile. The initial results from ATF showed that optimal operation[7] was achieved with the vacuum magnetic axis at $R = 2.05$ m, that is, 5 cm inward in major radius from the position of the standard ATF configuration. The existence of this optimal operational position for the vacuum magnetic axis is probably the combined consequence of the field errors and the plasma stability properties. The main consequences of the field errors[7] are the presence of a large 2/1 magnetic island, with a width of about 6 cm, and a high degree of field line stochasticity outside the $\iota = 0.5$ magnetic surface. As a function of the vacuum magnetic axis position, the average radius of the $\iota = 0.5$ surface has a maximum at about $R = 2.05$ m (Fig. 1). The field errors in ATF have been modeled in detail

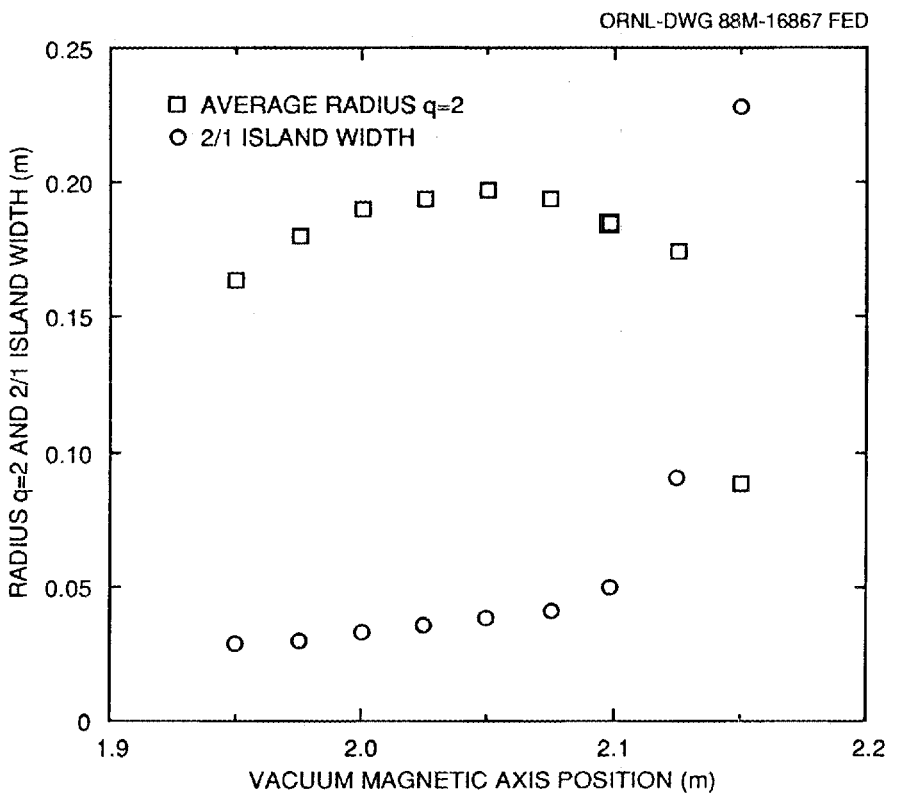

FIG. 1. Average radius of the $q = 2$ surface and estimate of 2/1 island size for ATF vacuum field with field error modeling of reference versus magnetic axis position.

by Harris and Lee.[9] Using their model and calculating the residue at the 0-point of the 2/1 magnetic island,[10] we can also estimate the width of the 2/1 island as a function of the vacuum magnetic axis position. The expression of the island width in terms of the residues is an approximation that is valid only for small widths, but it gives a more intuitive feeling of the effects of field error. When the width becomes very large ($R = 2.15$ m), it really means that the whole volume is filled with stochastic field lines. Figure 1 shows that the island width decreases when the vacuum magnetic axis is shifted inward.[7] Therefore, because the $m = 2$ island acts as an effective limiter, by shifting the axis inward to $R \approx 2.05$–2.00 m we maximize the effective plasma size and minimize the effect of field errors. However, as the vacuum magnetic axis keeps shifting inward in major radius, a magnetic hill builds up, making the plasma increasingly unstable. For inward shifts of the major radius of the order of 10 cm or larger ($R \leq 2.00$ m), most of the plasma confinement region should be unstable to ideal interchange modes at very low beta values, and, therefore, operation should lead to very poor confinement.

The pressure profile that we use is based on the reconstruction of the plasma parameters from Thomson scattering measurements.[11] All measured pressure profiles show two main characteristics: the pressure gradient is located at about half the expected plasma radius, and the profile is very steep. This position of the gradient is compatible with the $m = 2$ island being the effective limiter. Therefore, for estimates of ATF-A plasma properties we assume that this is the case. We take the average plasma radius to be reduced by a factor of 0.655 (position of the $\iota = 0.5$ surface) and the rotational transform at the edge to be $\iota = 0.5$ (Table I). For detailed MHD studies, we use the full plasma radius, $a_p = 27$ cm, placing a conducting wall at $\iota = 1.0$, and we use the reconstructed profile[11] at $\beta_0 \approx 2.5\%$ as the basic profile. Figure 2 shows the basic profile and the ATF-A rotational transform profile to indicate the positions of the most relevant rational surfaces. This experimental profile is well described by

$$p = p(0)\frac{1 - \tanh(12\psi - 1.56)}{1 + \tanh(1.56)} \quad , \tag{1}$$

where ψ is the poloidal flux function normalized to its plasma edge value. In Fig. 2, this profile is compared to the usual $p \sim (1 - \psi)^2$ profile that was regularly used in previous ATF stability studies.[4,12] In the present studies, to understand the systematics with beta, we maintain the pressure profile shape and change the value of peak beta. For these equilibrium calculations, we assume either zero current in

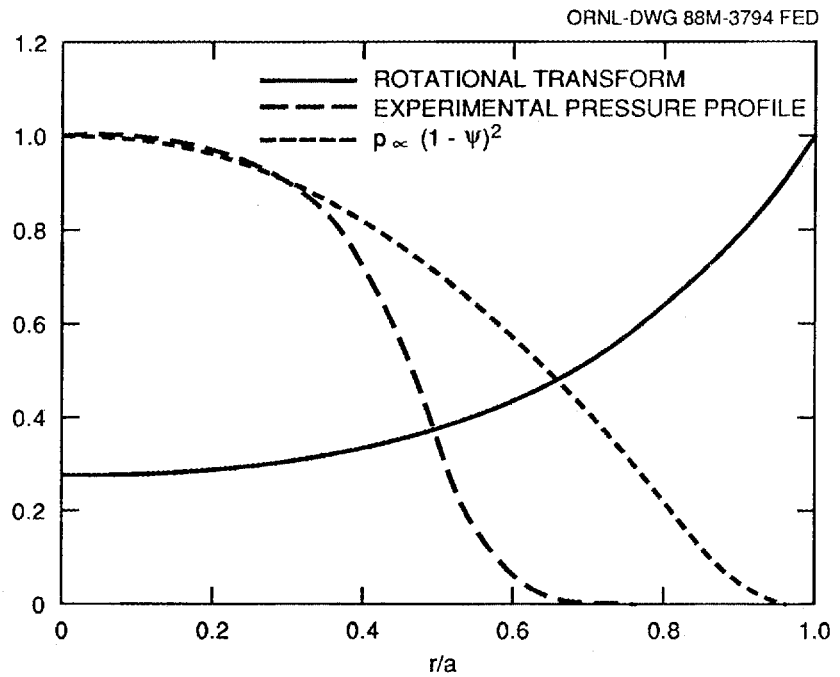

FIG. 2. Comparison of the pressure profile experimentally measured during the first phase of ATF operation and the pressure profile used in previous theoretical analysis. The vacuum rotational transform profile for the $R_0 =$ 2.05 m vacuum magnetic axis is also plotted.

each flux surface or flux conservation. The present ATF experimental data cannot discriminate between these options, and by doing the calculations both ways we have a measure of the sensitivity of the results to different assumptions.

The MHD equilibrium calculations have been done with the VMEC[13] and RSTEQ[14] codes. VMEC is a fully three-dimensional (3-D) code; its equilibrium result is used for the evaluation of the Mercier criterion.[15,16] RSTEQ is a two-dimensional (2-D) code based on the stellarator expansion approach;[17] the resulting equilibrium is used for low-n mode stability calculations. The equilibrium results of the two codes for the ATF configuration are very similar, as documented in the past.[4,12,18]

In Fig. 3, the shift of the magnetic axis shift as a function of beta has been plotted for the ATF-A configuration and for the standard ATF configuration with a 5-cm inward shift in major radius. The latter results are obtained using the standard profile $p \sim (1 - \psi)^2$. The figure shows that the shift for the ATF-A

configuration is larger, as could be expected. This enhanced shift effect for ATF-A is even more important than indicated by Fig. 3, because the shift plotted in this figure is normalized to the nominal ATF minor radius, while the effective minor radius of ATF-A is a factor of 0.655 smaller. With the conventional definition of the equilibrium beta limit as the beta value for which the magnetic axis shift is half of the minor radius, $\beta_0 \sim 8\%$ for ATF with the 5-cm inward shift and the $p \sim (1-\psi)^2$ profile. However, for the ATF-A configuration, the equilibrium beta limit is only $\beta_0 \sim 2\%$, once the effective reduction of the minor radius has been taken into account. These values for the equilibrium beta limit agree roughly with the scaling of the equilibrium beta limit as $\iota(a_p)^2/A_p$ (see Table I). Here A_p is the plasma aspect ratio. It is evident from these results that the effect of the field errors on the equilibrium properties of ATF is rather important. The equilibrium beta limit is reduced by a factor of four. The magnetic axis shift with beta, which basically scales as $\beta_0 A_p/\iota(a_p)^2$, is increased by the reduction of the minor radius and edge rotational transform. As a consequence, the magnetic well also deepens very rapidly with beta, as shown in Fig. 4; therefore, we can also expect changes in the stability properties of the configuration.

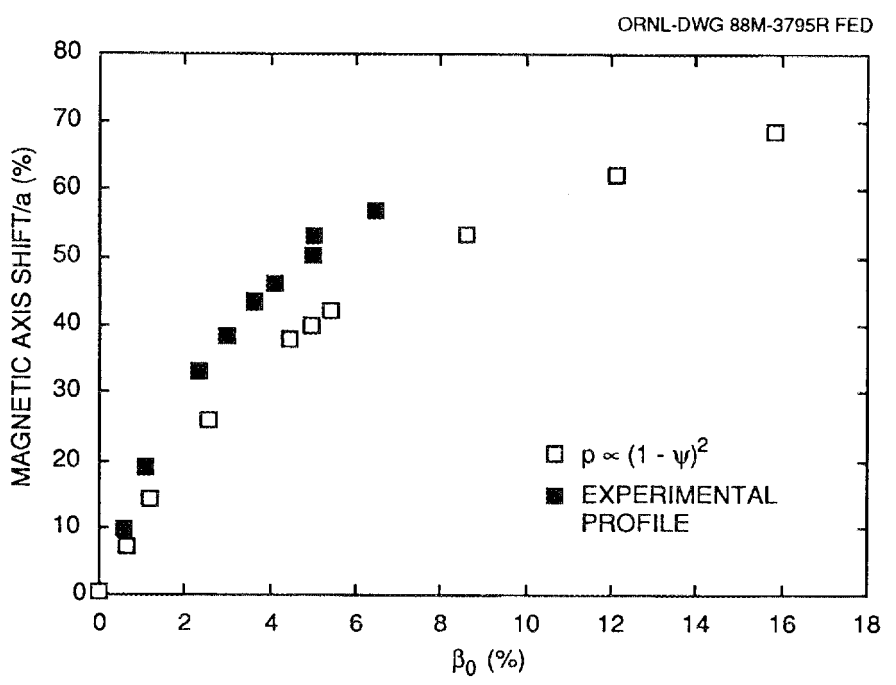

FIG. 3. Magnetic axis shift normalized to the average radius ($\bar{a} = 0.28$ m) versus peak beta for ATF for the pressure profile given in Eq. (1) and for $p \propto (1-\psi)^2$.

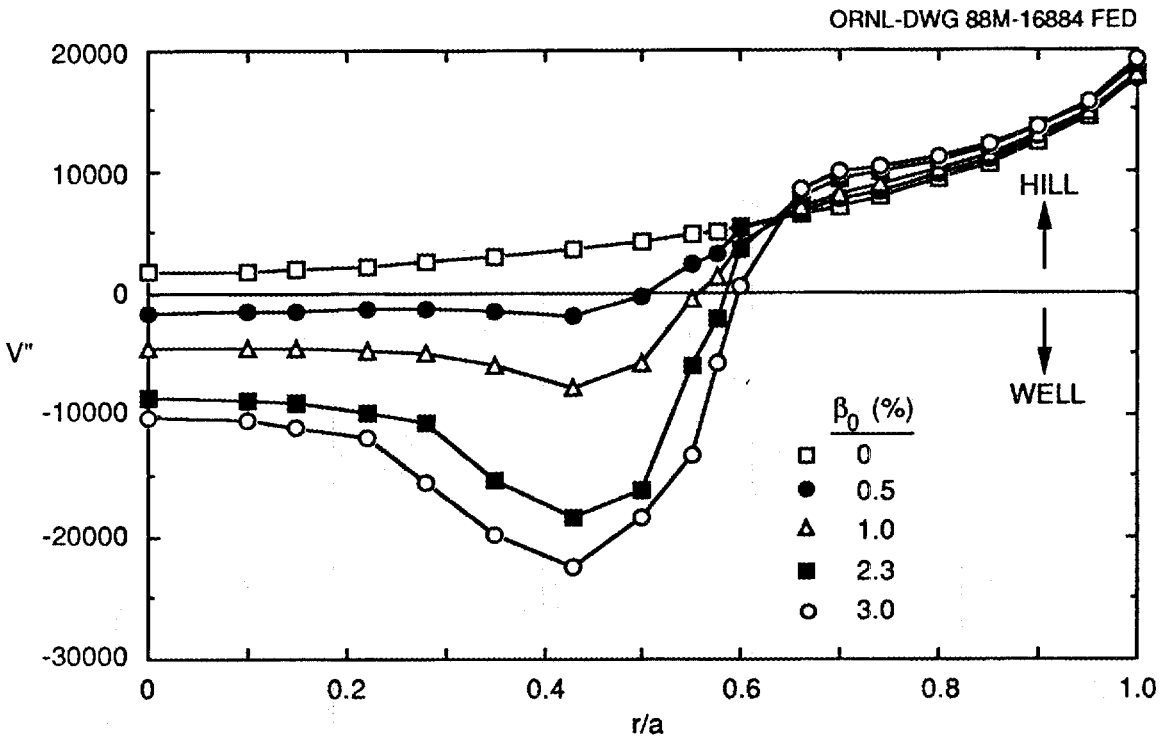

FIG. 4. V'', normalized to $R_0 B_0^2$, versus average radius for different peak beta values. The equilibrium calculations are for zero current and the pressure profile of Eq. (1).

The conventional definition of the equilibrium beta limit is useful for comparing the properties of different configurations, but it is an arbitrary definition. It is not based on any direct effect on confinement. The present ATF experimental results show that peak beta values above 3% have been achieved for the profiles considered in this analysis. At these beta values, the experiment showed no dramatic changes in confinement. Therefore, the actual beta limit is higher than that assigned by the conventional definition to ATF-A. This result is clearly encouraging because we can expect a similar situation for ATF with no field errors. A more relevant definition of equilibrium beta limit for the case with zero current is the value of beta for which an axisymmetric separatrix appears inside the plasma. We can see in Fig. 5, where the average magnetic surfaces for different beta values have been plotted, that for ATF-A such a separatrix appears at $\beta_0 \sim 5\%$. This value of beta is higher than any of the values obtained in ATF to date. Thus, we do not yet have the experimental information to determine the impact on plasma confinement of generating such a separatrix or to make a reasonable estimate of the equilibrium beta limit for ATF.

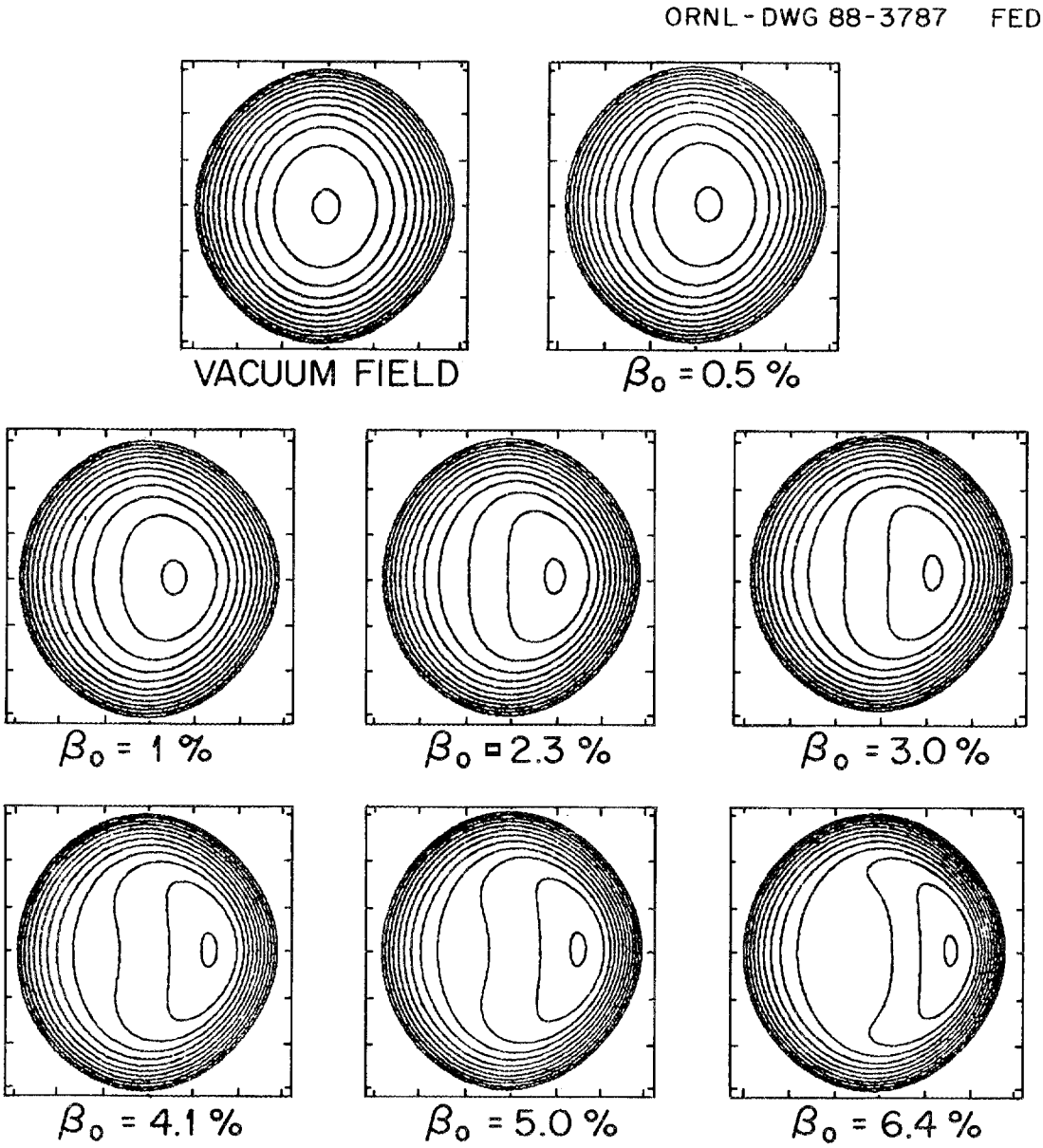

FIG. 5. Average magnetic surfaces in ATF, derived from stellarator expansion equilibria calculations with zero current and the pressure profile given by Eq. (1).

3. IDEAL MHD STABILITY PROPERTIES OF THE ATF-A CONFIGURATION

The equilibrium sequences described in Sect. 2 have been analyzed for their stability properties. To find the stability boundaries to ideal modes, the application of the 3-D Mercier criterion has been very useful. The reason is that for a configuration like ATF, the stability boundaries given by the low-n modes in general agree well with the boundaries of the Mercier modes,[18] because of the high degree of radial localization of the interchange modes for all n values. Therefore, we limit our discussion of stability to the Mercier stability criterion. The Mercier criterion[15,16] is expressed by

$$D_m \geq 0 \quad . \tag{2}$$

The particular normalization for D_m is given in Ref. 18.

Looking at a fixed radial position where the Mercier modes are most unstable and varying the value of beta, we can see that the transition to the second stability regime in ATF-A for Mercier modes happens at very low peak beta values ($\beta_0 \sim 1.3\%$). This is illustrated in Fig. 6, where D_m, at $r = 0.52$, is plotted versus peak

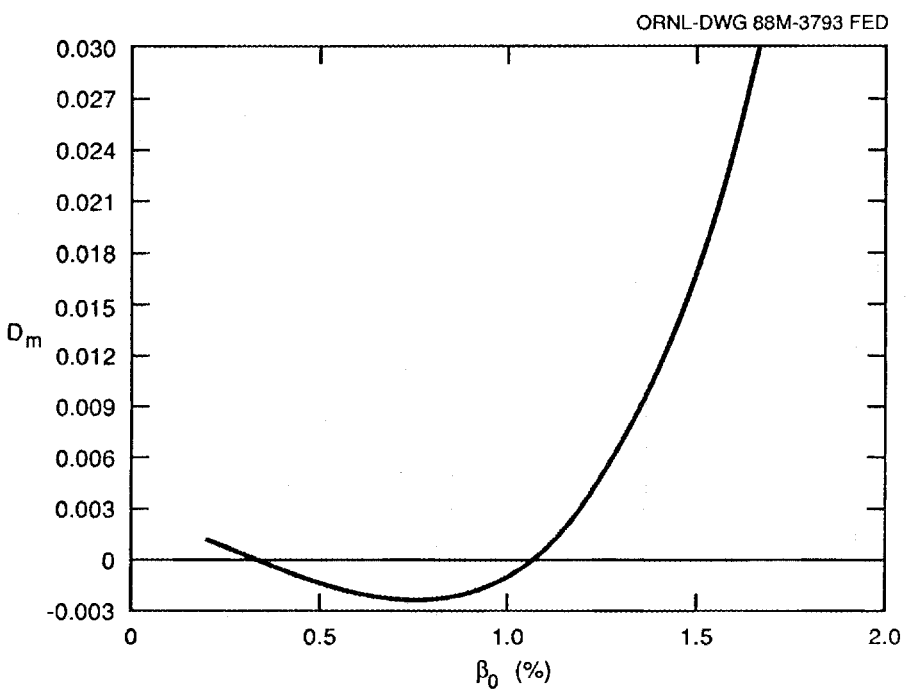

FIG. 6. 3-D Mercier criterion D_m, at a fixed average radius $r/\bar{a} = 0.56$, versus peak beta for zero-current equilibria with pressure profile given by Eq. (1).

beta. The rather strong beta self-stabilization effects are evident from the sharp rise of D_m with beta for $\beta_0 \geq 1.3\%$. This effect is not limited to a single radial point; instead, as can be seen in Fig. 7 for $\beta_0 \sim 1.3\%$, $D_m > 0$ over the whole radial range. Therefore, the plasma has accessed the second stability regime for this beta value. The Mercier stability results shown in Figs. 6 and 7 are for the zero-current equilibrium sequence. For flux-conserving equilibria, the magnetic axis shift with beta is smaller, and so are the beta self-stabilization effects. However, the Mercier stability boundaries do not change much, as shown in Fig. 8, and the threshold to the second stability regime increases only to $\beta_0 \sim 1.6\%$. The values of beta achieved in the experiment ($\beta_0 \geq 3\%$) are well above either of these threshold values.

It is interesting to find the lowest-n rational surfaces in the Mercier unstable region. They are indicated in Fig. 8 for both flux-conserving and zero-current equilibria. In both cases, the most relevant surfaces are $\iota = 2/5$, $\iota = 3/8$, and $\iota = 1/3$. Therefore, the low-n modes associated with these resonant surfaces are the most likely to be unstable. For the zero-current case [Fig. 8(a)], the rotational transform profile changes with increasing beta. First, the transform at the magnetic axis increases with β_0; that is why the $\iota = 1/3$ surface moves toward the axis until

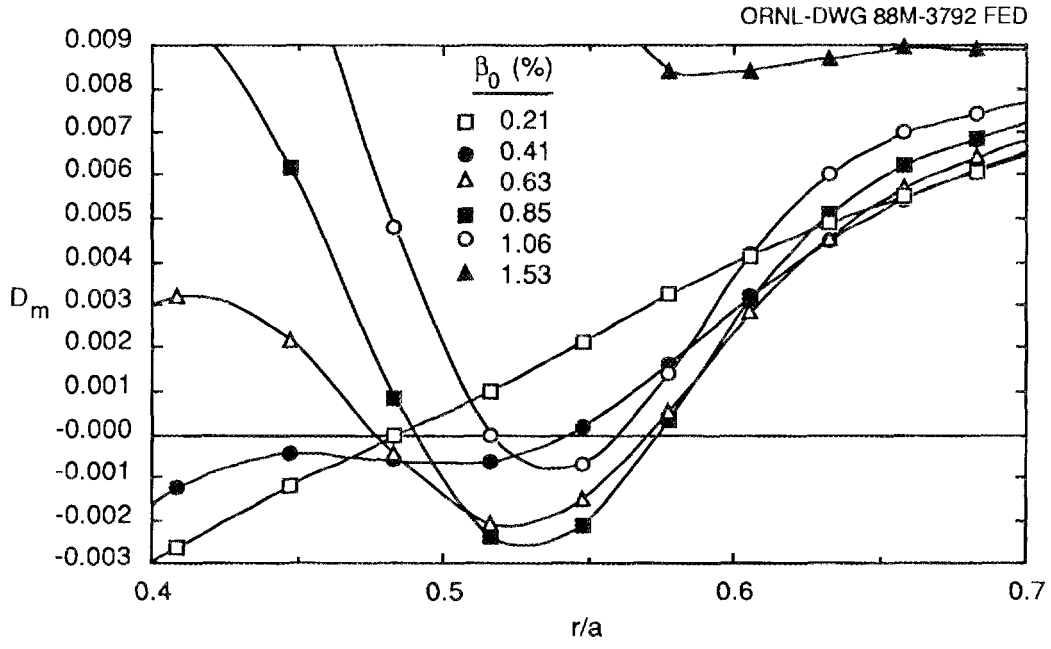

FIG. 7. 3-D Mercier criterion D_m versus average radius for zero-current equilibria with pressure profile given by Eq. (1) and different values of beta.

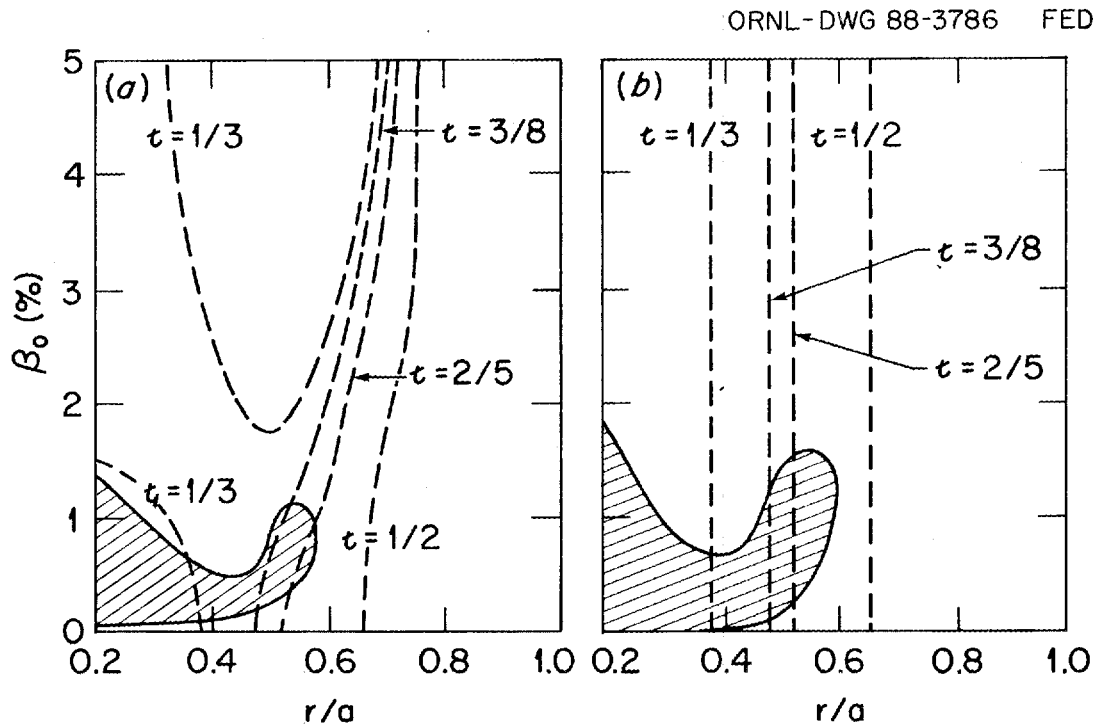

FIG. 8. 3-D Mercier unstable region (hatched) in the (β_0, r/a) plane for (a) zero-current and (b) flux-conserving equilibria. The positions of the most relevant low-n singular surfaces are also plotted. The pressure profile is given by Eq. (1), and the vacuum magnetic axis is at $R = 2.05$ m.

it disappears when $\iota(0) \geq 1/3$. For $\beta \geq 1.6\%$, ι decreases near the region of strong pressure gradient; the profile becomes double valued and its minimum value decreases with increasing beta. When min $\iota(r) \leq 1/3$, two $\iota = 1/3$ surfaces appear in the plasma. As β_0 keeps increasing, this minimum value of ι goes to zero, and that brings in an $n = 0$ separatrix, as discussed in Sect. 2.

The unstable Mercier regions shown in Fig. 8 have two distinct subregions, one at the plasma core and another localized around the pressure gradient region. The first one is not very important, in general, and can be eliminated by a slight flattening of the pressure profile at the core without much affecting the global confinement. The measurements of pressure profiles in the plasma core are not accurate enough for us to be sure whether this unstable region is real or not. The second region is more important because it cannot, in general, be eliminated by slightly changing the profile without changing the global confinement. For the

ATF-A configuration, the size of this unstable region is a sensitive function of the position of the vacuum magnetic axis. Shifting the major radius outward from $R = 2.05$ m by a few centimeters totally eliminates this unstable region. An inward shift greatly increases the size of the unstable region and can totally eliminate the second stable regime (Fig. 9). For the vacuum magnetic axis position at $R = 2.05$ m, the ideal unstable region is small, and so are the negative values of D_m in this region. However, this information is not sufficient to find out how weak the instability is in this region. A limitation of the Mercier criterion is that the value of D_m does not give a direct measure of the strength of the instability. One way to get some information is by examining the stability of low-n modes. We have used the FAR code,[14] which is based on the stellarator expansion, to evaluate the stability properties of the $n = 1$, 2, and 3 modes. The $n = 1$ mode is clearly stable, but the $n = 2$ and 3 modes, whose

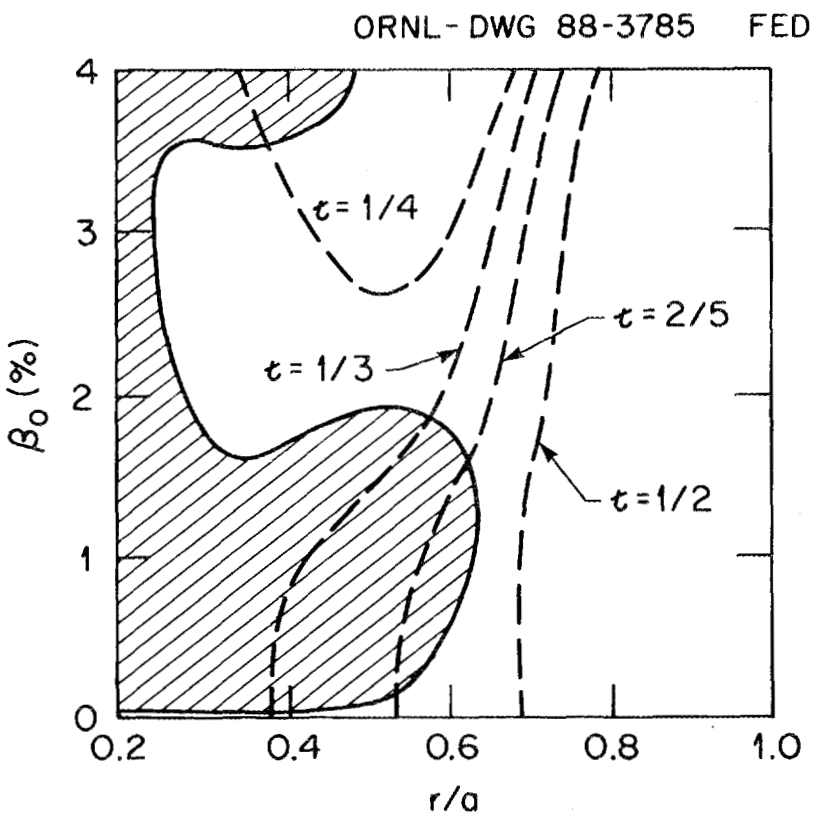

FIG. 9. 3-D Mercier unstable region (hatched) in the (β_0, r/a) plane for a zero-current equilibrium. The positions of the most relevant low-n singular surfaces are also plotted. The pressure profile is given by Eq. (1), and the vacuum magnetic axis is at $R = 2.00$ m.

dominant components are the $(m = 5; n = 2)$ and $(m = 8; n = 3)$, respectively, are so close to marginal stability that it has not been possible to obtain a converged linear growth rate for them. In this case, the ideal instability is weaker than a typical resistive interchange mode. Another way of estimating the importance of the unstable region is to evaluate how much the pressure profile must change to be marginally stable. To do so, we have parameterized the pressure profile as

$$p(r) = p(r)\left(p_1(r)/p_1(0) + c(1-\psi)(\psi-\psi_s)\exp\left\{-[(\psi-\psi_s)/W_s]^2\right\}\right) \qquad (3)$$

where $p_1(r)$ is given by Eq. (1). The parameters ψ_s, c, and W_s are determined from the Mercier marginal stability condition. For the ATF-A configuration with the vacuum magnetic axis at $R = 2.05$ m, the values $c = 3.0$ and $W_s = 0.2$ give a pressure profile that is stable for all β_0 values. This change of the pressure profile is very small (Fig. 10) and compatible with experimental errors. In contrast, when the vacuum magnetic axis is at $R = 2.00$ m, it is not possible to find a stable pressure profile close to the experimentally measured profile. Therefore, it is not surprising that access to the second stability regime has been relatively easy with the vacuum magnetic axis at $R = 2.05$ m. In conclusion, for the present ATF results, the only relevant instabilities in practice are the resistive interchange modes, which are considered in Sects. 4 and 5.

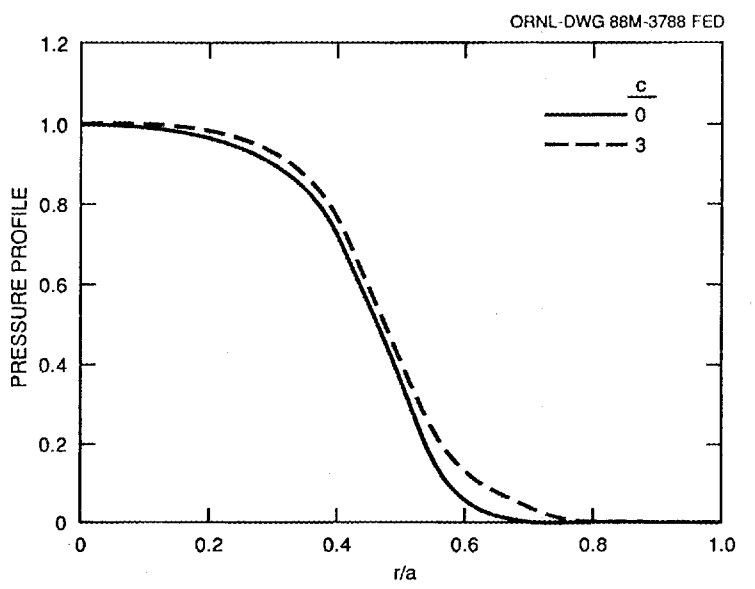

FIG. 10. Pressure profile given by Eq. (3) for $W_s = 0.2$ with $c = 0$ and with $c = 3$.

4. FLUCTUATION LEVEL IN ATF-A CAUSED BY RESISTIVE PRESSURE-GRADIENT-DRIVEN TURBULENCE

Resistive pressure-gradient-driven turbulence theory[19] is a convenient framework in which to begin analyzing the consequences of operation in the second stability regime. In Ref. 19, the nonlinear consequences of this instability are analyzed in detail. Here, we apply the results of this analysis to ATF parameters and include the beta self-stabilization effects. A simple model in cylindrical geometry was used to study resistive pressure-gradient-driven turbulence. The model is based on the equations

$$\frac{\partial \psi}{\partial t} = -R_0 \nabla_{\parallel} \phi + R_0 \eta J_z \quad , \tag{4}$$

$$\frac{dU}{dt} = -\frac{1}{\rho_m} \nabla_{\parallel} J_z + \frac{1}{\rho_m} \vec{z} \cdot (\nabla \Omega \times \nabla p) + \mu \nabla_{\parallel}^2 U \quad , \tag{5}$$

$$\frac{dp}{dt} = \chi_{\perp} \nabla_{\perp}^2 \tilde{p} - V_r \frac{dp_0}{dr} \quad . \tag{6}$$

Here ψ is the poloidal flux; ϕ the velocity stream function; $\tilde{p}$ the perturbed pressure; U the z-component of the vorticity, $U = \nabla_{\perp}^2 \phi$; and J_z the current parallel to the z-axis of the cylinder, $J_z = \nabla_{\perp}^2 \psi$.

This model can be regarded as the reduced set of MHD equations[20] for a stellarator configuration. This set of equations can be derived using the stellarator expansion.[17] From this point of view, the $\nabla\Omega$ term can be interpreted as the toroidally averaged curvature. At zero beta, this term includes only the average helical curvature, which is directly related to the toroidally varying part of the vacuum magnetic field $\vec{B}_v$ by

$$\Omega = \overline{\frac{|\vec{B}_v|^2}{B_0^2}} \quad , \tag{7}$$

where the bar indicates a toroidal angle average. In the present calculation, we do not consider the effect of the geodesic curvature; therefore, Ω is a function only of the average minor radius r. At finite beta, the effect of the magnetic axis shift must be included in the curvature term, and at lowest order in ϵ, we have

$$\Omega = \frac{2\Delta(r)}{R_0} + \overline{\frac{|\vec{B}_v|^2}{B_0^2}} \quad , \tag{8}$$

where $\Delta(r)$ is the average shift of each magnetic surface. In this case, it is better to express the average curvature in terms of the derivative of the specific volume, V', with respect to the toroidal flux, $B_0 r^2$,

$$\frac{d\Omega}{dr} = \frac{r}{a}\epsilon B_0^2 V'' \quad . \tag{9}$$

Here B_0 is the toroidal field strength, and V'' is a function of beta. As beta increases, the region in which $V'' < 0$ increases in radial extent, reducing the bad curvature region (Fig. 4).

The model given by Eqs. (4)–(6) does not include the stabilizing effects of compressibility or diamagnetic drift, the latter being more important. Therefore, this model is pessimistic in this sense. However, because of these simplifications, it can be used to perform detailed nonlinear calculations analytically as well as numerically. The numerical calculations can be done with enough resolution to separate relevant spatial scales and allow determination of the mode spectrum. This model has been a useful testbed for checking the analytical calculations and has allowed the identification of the basic turbulence saturation mechanism.[19]

The electrostatic potential and density fluctuations at saturation are given by the expressions[19]

$$\left\langle \frac{e\tilde{\Phi}}{T_e} \right\rangle_{\rm rms} = \left[\frac{\beta_0}{2\epsilon^2} \left(a\frac{d\Omega}{dr} \right) \left(\frac{-a}{p_0(0)} \frac{dp_0}{dr} \right) \right]^{5/6} \times \left(\frac{a^2 \mu_0 S}{\eta \tau_R} \right)^{1/3} \left(\frac{maqL_q}{r^2} \right)^{4/3} \left(\frac{eB\eta}{cT_e \mu_0} \right) \Lambda^{5/6} \quad , \tag{10}$$

$$\left\langle \frac{\tilde{n}}{n_0(0)} \right\rangle_{\rm rms} = \left[\frac{\beta_0}{2\epsilon^2} \left(a\frac{d\Omega}{dr} \right) \right]^{1/6} \left[\frac{-a}{p_0(0)} \frac{dp_0}{dr} \right]^{7/6} \left(\frac{\tau_R \eta}{a^2 \mu_0} \frac{1}{S} \right)^{1/3} \left(\frac{q^2 L_q^2}{mar} \right)^{1/3} \Lambda^{7/6} \quad . \tag{11}$$

Here, S is the Lundquist number, $L_q = |(1/q)(dq/dr)|^{-1}$, η is the resistivity, p_0 is the equilibrium pressure, m is the rms value of the poloidal mode number, the peak beta $\beta_0 = p_0(0)/(B_0^2/2\mu_0)$, a is the plasma minor radius, and $\epsilon = a/R_0$ is the inverse aspect ratio. The Λ enhancement factor depends weakly on the physics parameters and is the solution to the equation

$$\Lambda = \frac{2}{3\pi} \ln \left\{ \left[\frac{\beta_0}{2\epsilon^2} \left(a\frac{d\Omega}{dr} \right) \left(\frac{-a}{p_0(0)} \frac{dp_0}{dr} \right) \right]^{-1} \left(\frac{r^2}{maqL_q} \right)^4 128 \left(\frac{a^2 \mu_0}{\eta \tau_R} S \right)^2 \right\} - \frac{2}{\pi} \ln \Lambda \quad . \tag{12}$$

For the regime of interest in this paper, Λ varies only between 3 and 5. The physical meaning of this enhancement factor is discussed in Refs. 19 and 21.

The renormalization theory developed for the resistive pressure-gradient-driven turbulence is based on the electrostatic approximation to the model defined by Eqs. (4)–(6). The magnetic fluctuation can be inferred from the linearized Ohm's law and the calculated saturation level of the electrostatic potential, Eq. (10). However, one must be careful to treat the magnetic scale length accurately, as discussed in Ref. 22. The resulting fluctuation level for the magnetic fluctuations is given by

$$\left\langle \left| \frac{\widetilde{B}_r}{B_0} \right| \right\rangle_{\rm rms} = \left[\frac{\beta_0}{2\epsilon^2} \left(a \frac{d\Omega}{dr} \right) \left(\frac{-a}{p_0(0)} \frac{dp_0}{dr} \right) \right]^{7/6} \times \epsilon \left(\frac{a^2 \mu_0 S}{\eta \tau_R} \right)^{-1/3} \left(\frac{r}{ma} \right)^{1/3} \left(\frac{q L_q}{r} \right)^{5/3} \Lambda^{7/6} \quad . \tag{13}$$

In the expressions for the fluctuation level, Eqs. (10), (11), and (13), the beta effects are included in two ways. They appear explicitly as the driving term of the instability, $\beta_0(dp_0/dr)$, and indirectly in the curvature as the term $d\Omega/dr$, reducing the region of bad curvature as the axis shift increases. When the second effect, beta self-stabilization, overcomes the drive of the instability, the system is in the second stability regime. This explains why local measurements of the potential, density, or magnetic fluctuations serve as both a good monitor of the plasma properties and a way to experimentally determine the access to the second stability regime.

To calculate the fluctuation levels from Eqs. (10), (11), and (13), we need to know the electron temperature T_e, the ion temperature T_i, and the density n_0. To simplify the calculations, we take all profiles to be the same and to be given by Eq. (1). From the ATF data, we have extracted a scenario for the variation of $T_e(0)$, $T_i(0)$, and $n_0(0)$ with β_0 (see Fig. 11). In this way we can give a qualitative picture of the change of fluctuation level with β_0, which does not pretend to be accurate but only to illustrate the dominant trends. Detailed modeling, based on complete data sets, would be required for a more quantitative comparison of theory and experiment. Using the scenario of Fig. 11, we can calculate the fluctuation levels. In particular, using Eq. (13), we plot in Fig. 12 the magnetic fluctuation level as a function of r for different values of β_0. As beta increases, the magnetic well broadens, and the instability at the inner flux surfaces is suppressed as the position of $V'' = 0$ moves outward. At an inside fixed radial position, such as $r/a = 0.6$, we see the fluctuation level first go up with beta, then saturate at about $\beta_0 \sim 1\%$, and

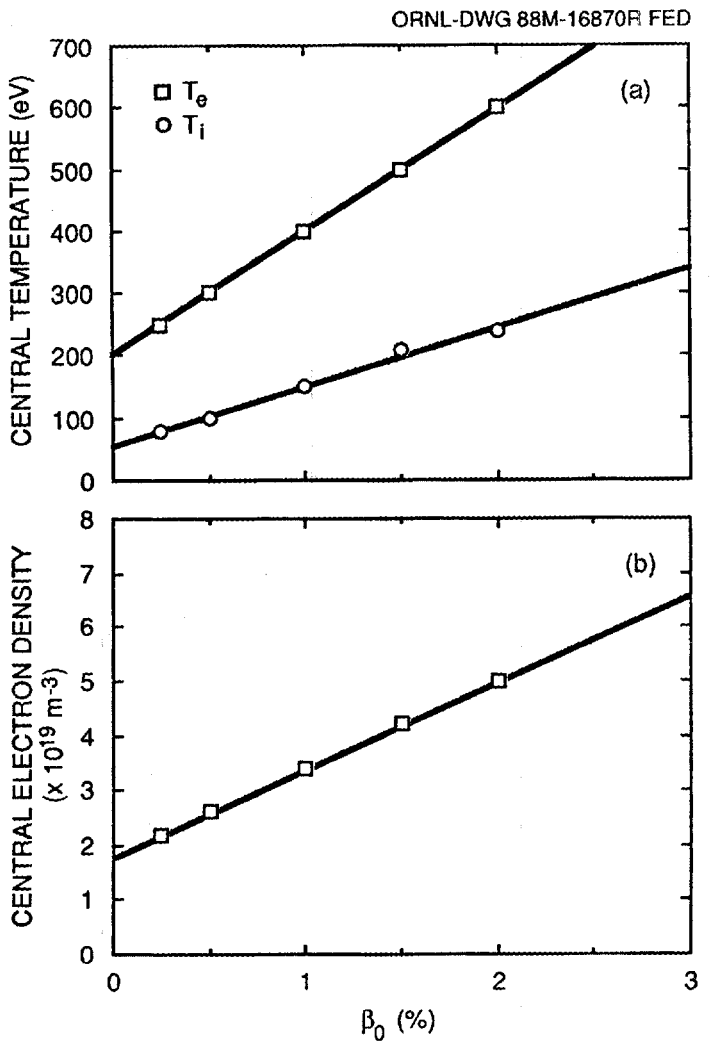

FIG. 11. Values of (a) electron temperature and ion temperature and (b) electron density versus peak beta for the transport scenario assumed in the calculation of fluctuation levels.

finally be stabilized for $\beta_0 \gtrsim 3\%$ (Fig. 13). For radial positions outside the main pressure gradient, such as $r/a = 0.7$, beta self-stabilization is not present (there is practically no beta there for the profile considered here). The situation is the same for density and potential fluctuations (Fig. 14). Notice that these fluctuations do not automatically die off when crossing to the second stability regime, but they do show the effects of beta self-stabilization. The maximum magnetic fluctuation levels are at radial positions $0.5 \leq r/a \leq 0.7$; this region encloses the marginally

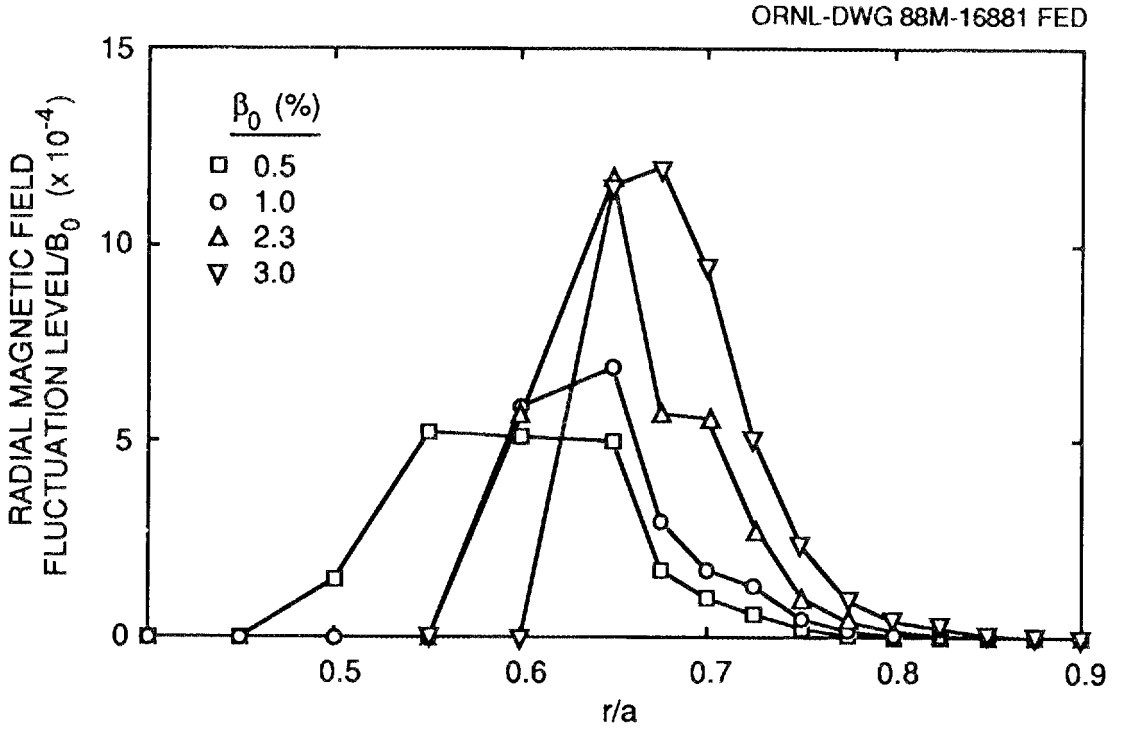

FIG. 12. Radial magnetic field fluctuation level, normalized to the toroidal field as given by Eq. (13), versus average radius for different values of peak beta.

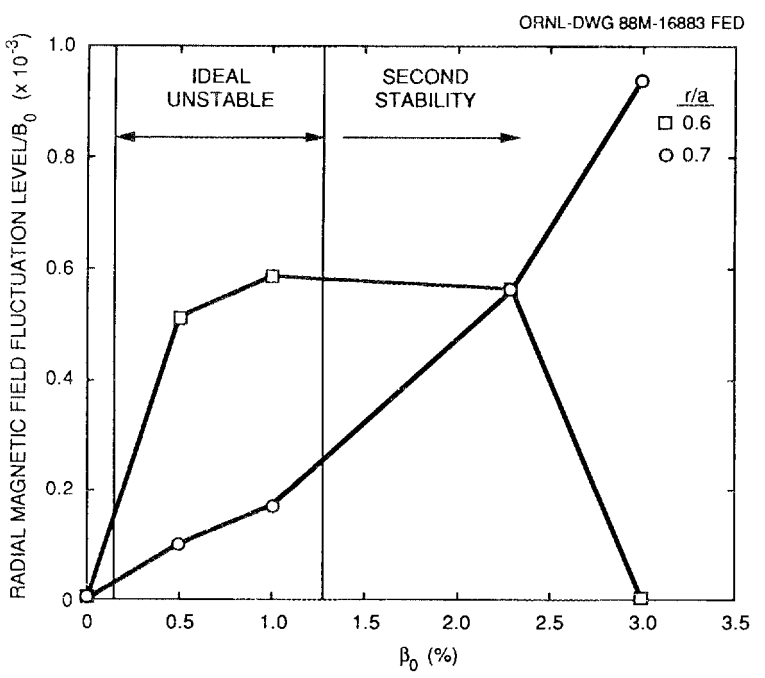

FIG. 13. Radial magnetic field fluctuation level, normalized to the toroidal magnetic field as given by Eq. (13), versus peak beta.

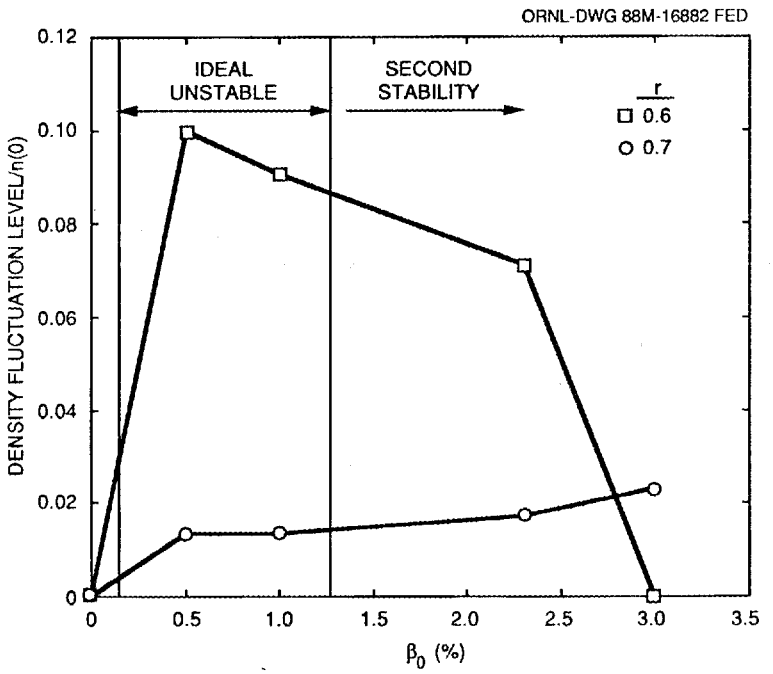

FIG. 14. Density fluctuation level, normalized to central density as given by Eq. (11), versus peak beta.

stable Mercier criterion. Therefore, resistive low-n modes with resonant surfaces in this radial range are the most likely cause of the experimentally observed magnetic fluctuations. Within experimental uncertainties, the fluctuation level does not seem to be very sensitive to profile effects. In Fig. 15, the radial magnetic field fluctuation level at $\beta_0 = 1.0\%$ is plotted for the two profiles of Fig. 10. The changes in the fluctuation level are rather small.

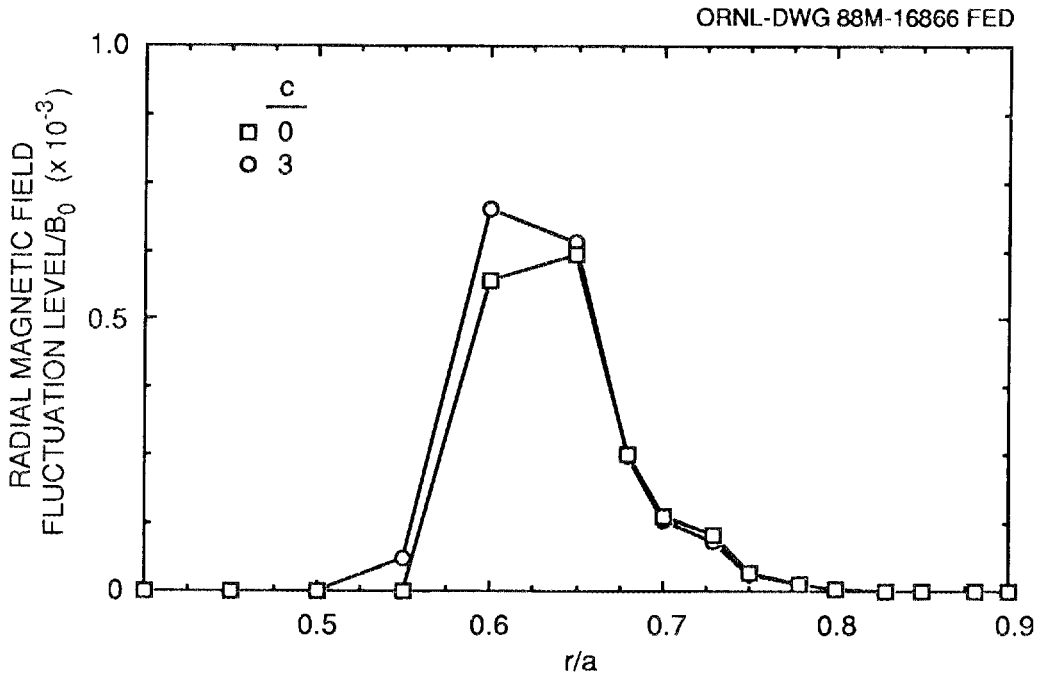

FIG. 15. Radial magnetic field fluctuation level, normalized to the toroidal magnetic field as given by Eq. (13), at $\beta_0 = 1.0\%$ for the two pressure profiles in Fig. 10.

5. LOW-n RESISTIVE INTERCHANGE INSTABILITY IN ATF-A

The linear stability properties of the resistive interchange modes have been studied with the FAR stability code,[23] which has been adapted to stellarator configurations[14] using the stellarator expansion approach. The stability of the $n = 1$, 2, and 3 modes has been investigated. The $n = 1$ growth rates are very small and difficult to converge; the dominant component is the $(m = 3; n = 1)$. This mode is strongly stabilized for $\beta_0 \geq 0.8\%$, as expected from inspection of Fig. 8. The $n = 2$ and 3 modes show clearly unstable features. For zero-current equilibria and $0.2\% \leq \beta_0 \leq 1.2\%$, the dominant component of the $n = 2$ mode is $(m = 5; n = 2)$, as could be expected from the marginal ideal stability properties of this mode. For $\beta_0 > 1.5\%$, the $(m = 6; n = 2)$ component becomes dominant; this corresponds to the β_0 values for which $\iota = 2/5$ is in the second stability regime. For the β_0 range studied, the linear growth rate as a function of β_0 first increases and then levels off for $\beta_0 \gtrsim 0.5\%$ [Fig. 16(a)]. However, the linear eigenfunction changes in such a way that the poloidal magnetic field fluctuation at the plasma edge, $\widetilde{B}_\theta(a)$, normalized to the maximum value of this fluctuating field component, decreases sharply for $\beta_0 > 1.0\%$ [Fig. 16(b)]. This change is caused by the change of the dominant component from $m = 5$ to $m = 6$.

We have a similar situation for the $n = 3$ mode. In this case, the dominant component is the $(m = 8; n = 3)$. The growth rate is higher than in the $n = 2$ case, but the normalized $\widetilde{B}_\theta(a)$ value is smaller.

The resistive interchange character of these modes is well established by the linear growth rate scaling with S, which shows the characteristic $S^{-1/3}$ power dependence. In all cases, the toroidal coupling is destabilizing, and the growth rate is larger than the predictions from cylindrical geometry, Eqs. (4)–(6). Although the toroidal coupling plays a very important role for these instabilities, the $\widetilde{B}_\theta$ spectrum at the plasma edge is clearly peaked at the dominant mode (Fig. 17).

For a first estimate of low-n fluctuation levels, we have used the model given by Eqs. (4)–(6) and implemented in the nonlinear initial value code KITE.[24] We are trying not to model in detail the experimental fluctuation measurements, but instead to show the basic traits of the theoretical predictions. To do a detailed modeling, diamagnetic and toroidal effects have to be included. From the linear results it is clear that the most relevant helicities are 3/1, 5/2, and 8/3. Let us consider the case of the 5/2 helicity. Modes from $(m = 5; n = 2)$ to $(m = 95; n = 38)$

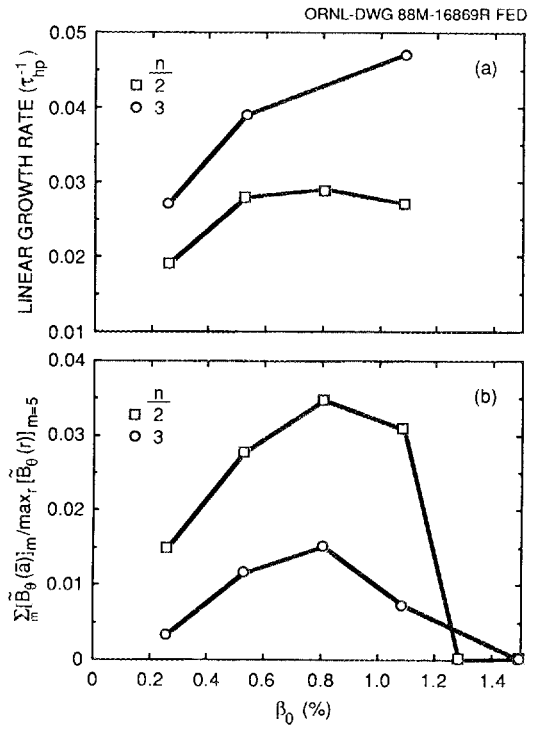

FIG. 16. Change of the linear stability properties of resistive interchange with peak β: (a) linear growth rate of the $n = 2$ and 3 modes, and (b) the corresponding values of $\sum_m \left[\widetilde{B}_\theta(\bar{a})\right]_m / \max_r \left[\widetilde{B}_\theta(r)\right]_{m=5}$ for these modes.

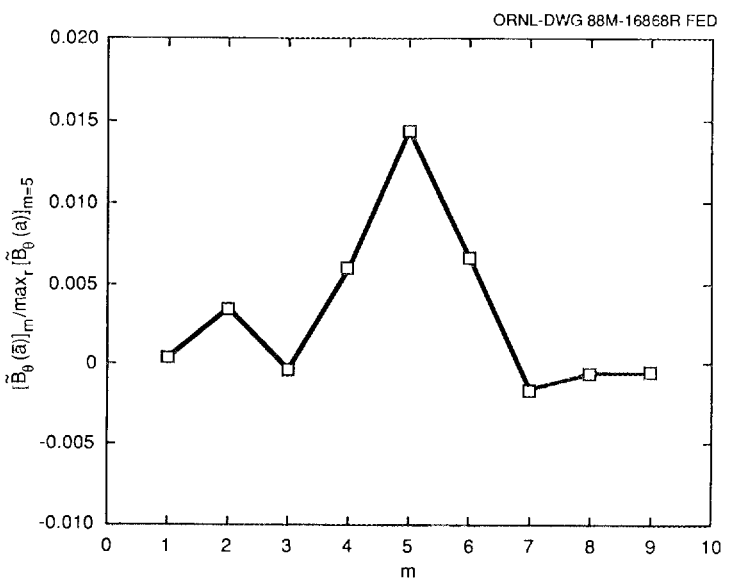

FIG. 17. Poloidal mode spectrum of the edge poloidal field fluctuation, $\left[\widetilde{B}_\theta(\bar{a})\right]_m / \max_r \left[\widetilde{B}_\theta(r)\right]_{m=5}$ for the $n = 2$ linear mode.

have been included in the calculation, with radial grids of $\Delta r = 10^{-3}$. The nonlinear evolution leads to a saturation of the instability with the spectrum dominated by the lowest-n mode. Although quasilinear effects are included, the saturation level is very close, within a factor of two, to the prediction of the analytic model of Sect. 4 based on the turbulent saturation of the modes. The saturation level as a function of beta shows a sharp increase, followed by saturation and a strong reduction of the fluctuation level. In Fig. 18, we have plotted the value of $\widetilde{B}_\theta(a)/B_0$ at saturation for the 5/2 helicity. The error bars reflect the spread during the time evolution of this level of fluctuations. The high values of $\widetilde{B}_\theta(a)/B_0$ for $0.4\% \leq \beta_0 \leq 0.9\%$ are due to the closeness to the ideal instability threshold. As we have already said, in this beta scan we have kept the same pressure profile, while in the experiment the pressure profile is somewhat narrower in the low-beta range.

Finally, when multiple helicity and toroidal effects are included, the saturation level of $\widetilde{B}(a)/B_0$ does not change much, but the mode spectrum changes in a significant way. Although the $(m = 5; n = 2)$ mode was the most unstable one linearly, the $\widetilde{B}(a)/B_0$ spectrum is dominated by the $(m = 2; n = 1)$ component (Fig. 19), which was linearly stable when the toroidal effects were turned off. These results agree with experimental fluctuation measurements, which also indicate that the spectrum is dominated by an $(m = 2; n = 1)$ component.

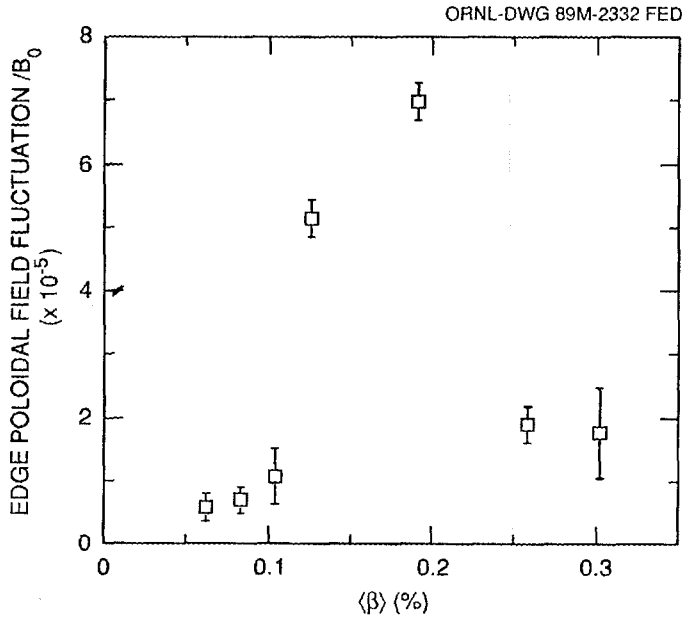

FIG. 18. $\widetilde{B}_\theta(\bar{a})/B_0$ at saturation for the 5/2 helicity as a function of beta.

A more detailed modeling of the fluctuation is required. The ω^* effects should be included for a more systematic comparison of theory and experiment.

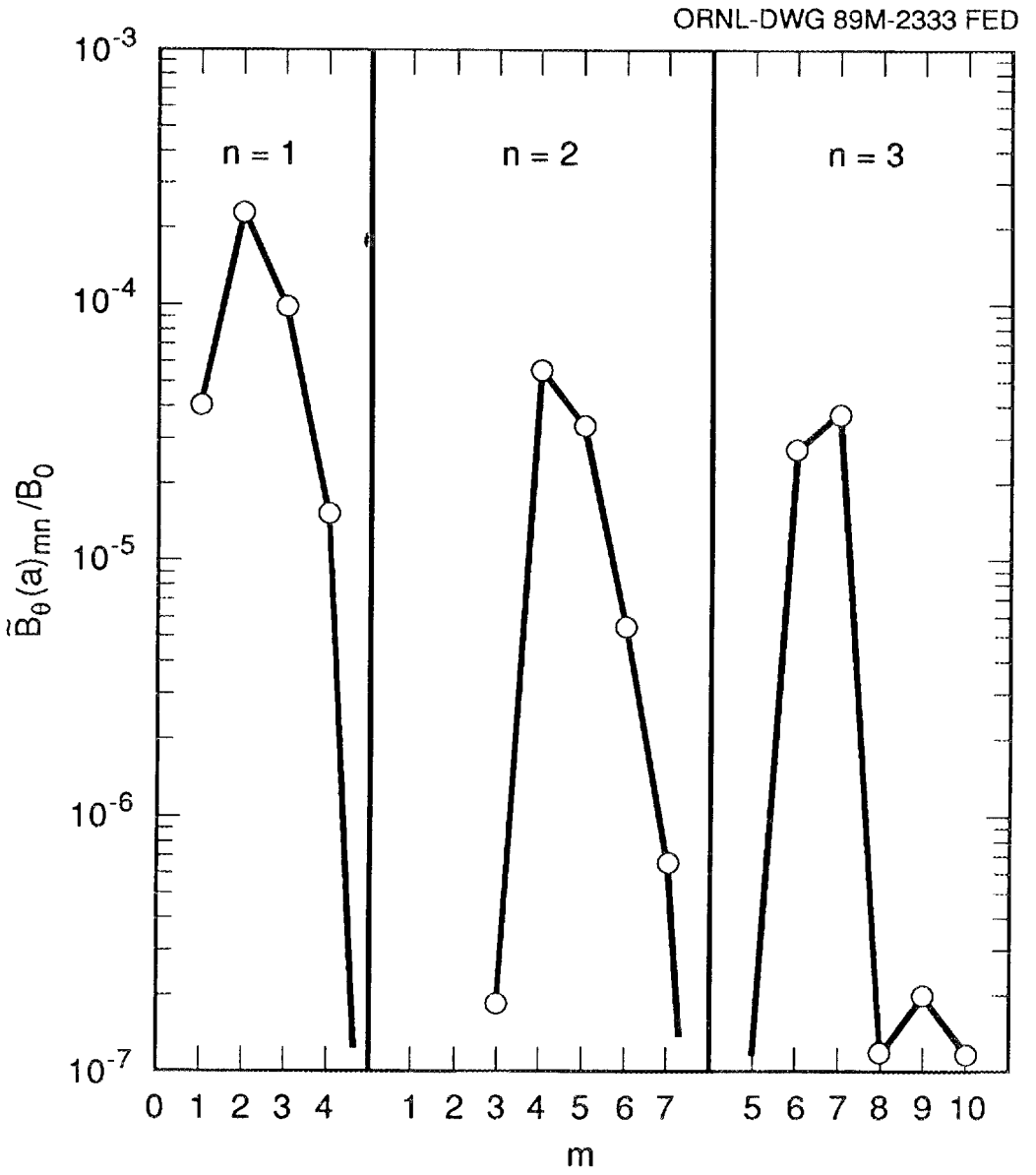

FIG. 19. $\widetilde{B}_\theta(a)/B_0$ spectrum at saturation for a multiple-helicity calculation including toroidal effects and a $\beta_0 = 0.26\%$ zero-current equilibrium with pressure profile given by Eq. (1).

6. DISCUSSION AND CONCLUSIONS

The purpose of this analysis is to paint a broad picture of how the MHD predictions for ATF change when the effect of field errors is taken into account. Neither the analysis nor the available data are complete. However, when both are put together, they do not show contradiction and give a very hopeful view of the potential performance of ATF. It is clear that we need more detailed data on profiles to make a detailed evaluation of the plasma stability properties. It is also very important to have density or potential fluctuation measurements inside the plasma. The magnetic fluctuation measurement, although very interesting, cannot give a full picture of the self-stabilization effect. On the theory side, we must develop a more complete model of the fluctuations by including diamagnetic and electric field effects.

Nevertheless, with the present information, we draw the following conclusions.

1. The answer to the question formulated in the introduction is probably: yes, the present data are compatible with ATF operation in the second stability regime, but it is not possible to prove it in a conclusive way.
2. Using a reduced plasma radius in ATF, although it reduces the boundaries of operation of the device (Fig. 20), can be a useful way of studying access to the second stability regime without adding substantial heating power.

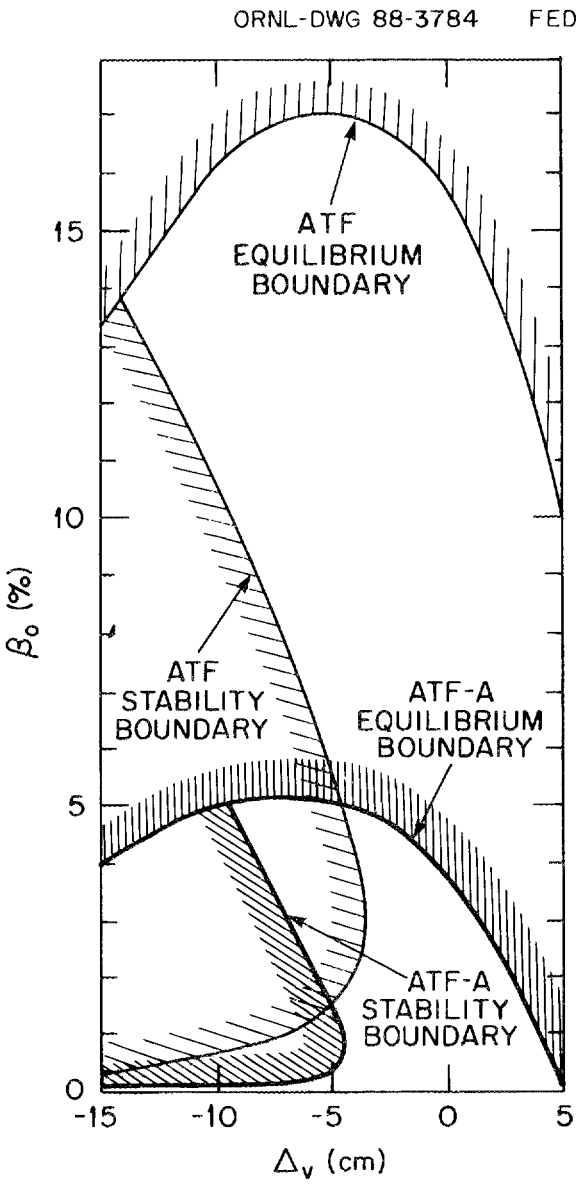

FIG. 20. ATF operational boundaries with and without field errors.

ACKNOWLEDGMENT

We are grateful to the ATF experimental group for providing us with unpublished data, and in particular to M. Murakami and J. H. Harris for many useful discussions of the data and their implications. We are also grateful to S. P. Hirshman for making available to us the VMEC code for calculation of 3-D equilibria.

REFERENCES

1. J. F. Lyon, B. A. Carreras, K. K. Chipley, M. J. Cole, J. H. Harris, T. C. Jernigan, R. L. Johnson, V. E. Lynch, B. E. Nelson, J. A. Rome, J. Sheffield, and P. B. Thompson, Fusion Technol. **10**, 179 (1986).
2. B. Coppi, A. Ferreira, J. W. Mark, and J. J. Ramos, Nucl. Fusion **19**, 715 (1979).
3. A. B. Mikhailovskii and V. D. Shafranov, Zh. Eksp. Teor. Fiz. **66**, 190 (1974) [Sov. Phys. JETP **39**, 88 (1974)]; L. M. Kovrizhnykh and S. V. Shchepetov, Sov. J. Plasma Phys. **6**, 533 (1980).
4. B. A. Carreras, H. R. Hicks, J. A. Holmes, V. E. Lynch, L. Garcia, J. H. Harris, T. C. Hender, and B. F. Masden, Phys. Fluids **26**, 3569 (1983).
5. H. P. Furth, J. Killeen, and M. N. Rosenbluth, Phys. Fluids **6**, 77 (1963).
6. B. A. Carreras, Comments Plasma Phys. Controlled Fusion **12**, 35 (1988).
7. M. J. Saltmarsh et al., "Initial Results from the ATF Torsatron," paper IAEA-CN-50/C-1-2 presented at the 12th International Conference on Plasma Physics and Controlled Nuclear Fusion Research, Nice, October 12–19, 1988 (proceedings to be published by the International Atomic Energy Agency).
8. J. H. Harris et al., Bull. Am. Phys. Soc. **33**, 2070 (1988).
9. J. H. Harris and D. K. Lee, private communiation.
10. J. R. Cary and J. D. Hanson, Phys. Fluids **29**, 2464 (1986).
11. M. Murakami, B. A. Carreras, J. H. Harris, F.S.B. Anderson, G. L. Bell, J. D. Bell, T. S. Bigelow, R. J. Colchin, E. C. Crume, N. Dominguez, J. L. Dunlap, A. C. England, J. C. Glowienka, L. D. Horton, H. C. Howe, R. C. Isler, H. Kaneko, R. R. Kindsfather, J. N. Leboeuf, V. E. Lynch, M. M. Menon, R. N. Morris, G. H. Neilson, V. K. Paré, D. A. Rasmussen, J. B. Wilgen, and W. R. Wing, "Second Stability Studies in the ATF Torsatron," paper presented at the 16th European Conference on Controlled Fusion and Plasma

Physics, Venice, March 13–17, 1989 (proceedings to be published by the European Physical Society).

12. T. C. Hender, B. A. Carreras, L. A. Charlton, L. Garcia, H. R. Hicks, J. A. Holmes, and V. E. Lynch, Nucl. Fusion **25**, 1463 (1985).

13. S. P. Hirshman, W. I. van Rij, and P. Merkel, Comput. Phys. Comm. **43**, 143 (1986).

14. V. E. Lynch, B. A. Carreras, L. A. Charlton, L. Garcia, T. C. Hender, H. R. Hicks, and J. A. Holmes, J. Comput. Phys. **66**, 41 (1986).

15. C. Mercier, Nucl. Fusion **1**, 47 (1960).

16. J. M. Greene and J. L. Johnson, Phys. Fluids **4**, 510 (1962).

17. J. M. Greene and J. L. Johnson, Phys. Fluids **4**, 875 (1961).

18. N. Dominguez, J. N. Leboeuf, B. A. Carreras, and V. E. Lynch, "Ideal Low-n and Mercier Mode Stability Boundaries for $\ell = 2$ Torsatrons," ORNL/P-89/1086, Martin Marietta Energy Systems, Inc., Oak Ridge National Laboratory, March 1989 [submitted to Nucl. Fusion (1989)].

19. B. A. Carreras, L. Garcia, and P. H. Diamond, Phys. Fluids **30**, 1388 (1987).

20. H. R. Strauss, Plasma Phys. **22**, 633 (1980).

21. P. H. Diamond and B. A. Carreras, Comments Plasma Phys. Controlled Fusion **10**, 271 (1987).

22. B. A. Carreras and P. H. Diamond, "Thermal Diffusivity Induced by Resistive Pressure-Gradient-Driven Turbulence," ORNL/P-88/2656, Martin Marietta Energy Systems, Inc., Oak Ridge National Laboratory, August 1988 [accepted for publication in Phys. Fluids B (1989)].

23. L. A. Charlton, J. A. Holmes, H. R. Hicks, V. E. Lynch, and B. A. Carreras, J. Comput. Phys. **63**, 107 (1986).

24. L. Garcia, H. R. Hicks, B. A. Carreras, L. A. Charlton, and J. A. Holmes, J. Comput. Phys. **65**, 253 (1986).

ORNL/TM-11102
Dist. Category UC-427

INTERNAL DISTRIBUTION

1. D. B. Batchelor
2–6. B. A. Carreras
7. M. D. Carter
8. E. C. Crume
9–13. N. O. Dominguez
14. R. A. Dory
15. C. L. Hedrick
16. S. P. Hirshman
17. J. T. Hogan
18. W. A. Houlberg
19. H. C. Howe
20. E. F. Jaeger
21–25. J-N. Leboeuf
26. G. S. Lee
27–31. J. F. Lyon
32. J. A. Rome
33. K. C. Shaing
34. J. Sheffield
35. D. A. Spong
36–37. Laboratory Records Department
38. Laboratory Records, ORNL–RC
39. Document Reference Section
40. Central Research Library
41. Fusion Energy Division Library
42–43. Fusion Energy Division Publications Office
44. ORNL Patent Office

EXTERNAL DISTRIBUTION

45. Office of the Assistant Manager for Energy Research and Development, U.S. Department of Energy, Oak Ridge Operations Office, P. O. Box 2001, Oak Ridge, TN 37831-8600
46. J. D. Callen, Department of Nuclear Engineering University of Wisconsin Madison, WI 53706-1687
47. J. F. Clarke, Director, Office of Fusion Energy, Office of Energy Research, ER-50 Germantown, U.S. Department of Energy, Washington, DC 20545
48. R. W. Conn, Department of Chemical, Nuclear, and Thermal Engineering, University of California, Los Angeles, CA 90024
49. S. O. Dean, Fusion Power Associates, 2 Professional Drive, Suite 248, Gaithersburg, MD 20879
50. H. K. Forsen, Bechtel Group, Inc., Research Engineering, P. O. Box 3965, San Francisco, CA 94105
51. J. R. Gilleland, L-644, Lawrence Livermore National Laboratory, P.O. Box 5511, Livermore, CA 94550
52. R. W. Gould, Department of Applied Physics, California Institute of Technology, Pasadena, CA 91125
53. R. A. Gross, Plasma Research Laboratory, Columbia University, New York, NY 10027
54. D. M. Meade, Princeton Plasma Physics Laboratory, P.O. Box 451, Princeton, NJ 08544
55. M. Roberts, International Programs, Office of Fusion Energy, Office of Energy Research, ER-52 Germantown, U.S. Department of Energy, Washington, DC 20545
56. W. M. Stacey, School of Nuclear Engineering and Health Physics, Georgia Institute of Technology, Atlanta, GA 30332

57. D. Steiner, Nuclear Engineering Department, NES Building, Tibbetts Avenue, Rensselaer Polytechnic Institute, Troy, NY 12181
58. R. Varma, Physical Research Laboratory, Navrangpura, Ahmedabad 380009, India
59. Bibliothek, Max-Planck Institut für Plasmaphysik, Boltzmannstrasse 2, D-8046 Garching, Federal Republic of Germany
60. Bibliothek, Institut für Plasmaphysik KFA Jülich GmbH, Postfach 1913, D-5170 Jülich, Federal Republic of Germany
61. Bibliothek, KfK Karlsruhe GmbH, Postfach 3640, D-4500 Karlsruhe 1, Federal Republic of Germany
62. Bibliotheque, Centre de Recherches en Physique des Plasmas, 21 Avenue des Bains, CH-1007 Lausanne, Switzerland
63. R. Aymar, CEN/Cadarache, Departement de Recherches sur la Fusion Contrôlée, F-13108 Saint-Paul-lez-Durance Cedex, France
64. Bibliothèque, CEN/Cadarache, F-13108 St.-Paul-lez-Durance, Cedex, France
65. Library, Culham Laboratory, UKAEA, Abingdon, Oxfordshire, OX14 3DB, England
66. Library, JET Joint Undertaking, Abingdon, Oxfordshire, OX14 3EA, England
67. Library, FOM-Instituut voor Plasma-Fysica, Rijnhuizen, Edisonbaan 14, 3439 MN Nieuwegein, The Netherlands
68. Library, Institute of Plasma Physics, Nagoya University, Nagoya 464, Japan
69. Library, International Centre for Theoretical Physics, P.O. Box 586, I-34100 Trieste, Italy
70. Library, Centro Richerche Energia Frascati, C.P. 65, I-00044 Frascati (Roma), Italy
71. Library, Plasma Physics Laboratory, Kyoto University, Gokasho, Uji, Kyoto 611, Japan
72. Plasma Research Laboratory, Australian National University, P.O. Box 4, Canberra, A.C.T. 2601, Australia
73. Library, Japan Atomic Energy Research Institute, Naka Fusion Research Establishment, 801-1 Mukoyama, Naka-machi, Naka-gun, Ibaraki-ken, Japan
74. G. A. Eliseev, I. V. Kurchatov Institute of Atomic Energy, P.O. Box 3402, 123182 Moscow, U.S.S.R.
75. V. A. Glukhikh, Scientific-Research Institute of Electro-Physical Apparatus, 188631 Leningrad, U.S.S.R.
76. I. Shpigel, Institute of General Physics, U.S.S.R. Academy of Sciences, Ulitsa Vavilova 38, Moscow, U.S.S.R.
77. D. D. Ryutov, Institute of Nuclear Physics, Siberian Branch of the Academy of Sciences of the U.S.S.R., Sovetskaya St. 5, 630090 Novosibirsk, U.S.S.R.
78. V. T. Tolok, Kharkov Physical-Technical Institute, Academical St. 1, 310108 Kharkov, U.S.S.R.
79. Deputy Director, Southwestern Institute of Physics, P.O. Box 15, Leshan, Szichuan, China (PRC)
80. Director, Institute of Plasma Physics, P.O. Box 26, Hefei, Anhui, China (PRC)
81. D. Crandall, Experimental Plasma Research Branch, Division of Development and Technology, Office of Fusion Energy, Office of Energy Research, ER-542 Germantown, U.S. Department of Energy, Washington, DC 20545
82. N. A. Davies, Office of the Associate Director, Office of Fusion Energy, Office of Energy Research, ER-51 Germantown, U.S. Department of Energy, Washington, DC 20545
83. R. H. McKnight, Experimental Plasma Research Branch, Division of Development and Technology, Office of Fusion Energy, Office of Energy Research, ER-51 Germantown, U.S. Department of Energy, Washington, DC 20545

84. D. B. Nelson, Director, Division of Applied Plasma Physics, Office of Fusion Energy, Office of Energy Research, ER-54 Germantown, U.S. Depart ment of Energy, Washington, DC 20545
85. E. Oktay, Division of Confinement Systems, Office of Fusion Energy, Office of Energy Research, ER-55 Germantown, U.S. Department of Energy, Washington, DC 20545
86. W. Sadowski, Fusion Theory and Computer Services Branch, Division of Applied Plasma Physics, Office of Fusion Energy, Office of Energy Research, ER-541 Germantown, U.S. Department of Energy, Washington, DC 20545
87. R. E. Mickens, Atlanta University, Department of Physics, Atlanta, GA 30314
88. M. N. Rosenbluth, University of California at San Diego, La Jolla, CA 92093
89. Duk-In Choi, Department of Physics, Korea Advanced Institute of Science and Technology, P.O. Box 150, Chong Ryang-Ri, Seoul, Korea
90. Library of the Physics Department, University of Ioannina, Ioannina, Greece
91. C. De Palo, Library, Associazione EURATOM-ENEA sulla Fusione, C.P. 65, Frascati (Roma), Italy
92. Theory Department Read File, c/o D. W. Ross, University of Texas, Institute for Fusion Studies, Austin, TX 78712
93. Theory Department Read File, c/o R. Parker, Director, Plasma Fusion Center, NW 16-202, Massachusetts Institute of Technology, Cambridge, MA 02139
94. Theory Department Read File, c/o R. White, Princeton Plasma Physics Laboratory, P.O. Box 451, Princeton, NJ 08544
95. Theory Department Read File, c/o L. Kovrizhnykh, Lebedev Institute of Physics, Academy of Sciences, 53 Leninsky Prospect, 117924 Moscow, U.S.S.R.
96. Theory Department Read File, c/o B. B. Kadomtsev, I. V. Kurchatov Institute of Atomic Energy, P.O. Box 3402, 123182 Moscow, U.S.S.R.
97. Theory Department Read File, c/o T. Kamimura, Institute of Plasma Physics, Nagoya University, Nagoya 464, Japan
98. Theory Department Read File, c/o C. Mercier, Departemente de Recherches sur la Fusion Contrôlée, B.P. 6, F-92260 Fontenay-aux-Roses (Seine), France
99. Theory Department Read File, c/o T. E. Stringer, JET Joint Undertaking, Culham Laboratory, Abingdon, Oxfordshire OX14 3EA, England
100. Theory Department Read File, c/o R. Briscoe, Culham Laboratory, Abingdon, Oxfordshire OX14 3DB, England
101. Theory Department Read File, c/o D. Biskamp, Max-Planck-Institut für Plasmaphysik, Boltzmannstrasse 2, D-8046 Garching, Federal Republic of Germany
102. Theory Department Read File, c/o T. Takeda, Japan Atomic Energy Research Institute, Tokai Establishment, Tokai-mura, Naka-gun, Ibaraki-ken, Japan
103. Theory Department Read File, c/o J. Greene, General Atomics, P.O. Box 81608, San Diego, CA 92138
104. Theory Department Read File, c/o L. D. Pearlstein, L-630, Lawrence Livermore National Laboratory, P.O. Box 5511, Livermore, CA 94550
105. Theory Department Read File, c/o R. Gerwin, CTR Division, Los Alamos National Laboratory, P.O. Box 1663, Los Alamos, NM 87545
106. J. L. Johnson, Plasma Physics Laboratory, Princeton University, P.O. Box 451, Princeton, NJ 08543
107. O. Motojima, Plasma Physics Laboratory, Kyoto University, Gokasho, Uji, Kyoto, Japan
108. D. Schnack, SAIC, 10260 Campus Point Drive, San Diego, CA 92121
109. V. D. Shafranov, I. V. Kurchatov Institute of Atomic Energy, P.O. Box 3402, 123182 Moscow, U.S.S.R.
110. J. L. Shohet, Torsatron/Stellarator Laboratory, University of Wisconsin, Madison, WI 53706

111. H. Wobig, Max-Planck-Institut für Plasmaphysik, Boltzmannstrasse 2, D-8046 Garching, Federal Republic of Germany
112–157. Given distribution according to OSTI-4500, Magnetic Fusion Energy (Category Distribution UC-427, Theoretical Plasma Physics)